Supporting Information

Supramolecular Radical Cation: Folding-Enhanced Electrostatic Effect for Promoting Radical-Mediated Oxidation

Bohan Tang, Wan-Lu Li, Yang Jiao, Jun-Bo Lu, Jiang-Fei Xu, Zhiqiang Wang, Jun Li* and Xi Zhang*

1. General instrumentation and methods.

The ^{1}H NMR spectra were obtained using a JOEL JNM-ECA400 apparatus, while the 2D ROESY spectrum was obtained using a JOEL JNM-ECA600 apparatus. The UV/Vis spectra were measured using a HITACHI U-3010 spectrophotometer. For all the UV-Vis spectra, path length was 10.0 mm.

The Fenton reagents used in this work contained two components: 50 mM $FeCl_3$ aqueous solution (containing 1 M HCl to avoid hydrolysis) and 500 mM H_2O_2 aqueous solution. As a typical process, 2 μL $FeCl_3$ solution and 10 μL H_2O_2 solution were added into DPP or DPP/(CB[7])$_2$ aqueous solution (0.1 mM, 1 mL), respectively. After a rapid mixing, the solution was immediately placed at a constant temperature to undergo Fenton oxidation. The reaction kinetics was monitored with the variation of UV/Vis absorption.

Electronic paramagnetic resonance (EPR) measurements were performed on a JEOL JES-FA200 apparatus, with 9057 MHz microwave frequency and 4.00 mW power.

Isothermal titration calorimetry (ITC) experiments were carried out with a Microcal VP-ITC apparatus in acetate buffer solution (50 mM pH 4.75) at 298.15 K.

2. Synthesis of DPP derivatives.

2.1 Synthesis of DPP

3,6-Diphenyl-2,5-dihydropyrrolo[3,4-c]pyrrole-1,4-dione (0.5 g, 1.73 mmol) and 4.16 mmol NaH (~2.4 equivalent) were added into 15 mL anhydrous DMF. The mixture was stirred until there was no bubble of H_2 generated anymore. Then 1,8-dibromooctane (3.2 mL, 17.4 mmol) was added. The reaction mixture was continued stirring overnight at 85 °C. After being cooled to room temperature, the reaction mixture was instilled into water and extracted by diethyl ether for three times. Then the diethyl ether phase was collected, washed with water for two times and dried with Na_2SO_4 for 3 h. The solution was filtered and the solvent was evaporated. The crude product was further purified using silica gel column chromatography with the solution of CH_2Cl_2:$CH_3COOC_2H_5$ = 20:1 as eluent to result in an orange powder (Compound 1). The yield was 40%.

^{1}H NMR (400 MHz, DMSO-d6, 25 °C, TMS): 7.80~7.85 (m, 4H), 7.56~7.64 (m, 6H), 3.71 (t, J = 7.2 Hz, 4H), 3.48 (t, J = 6.7 Hz, 4H), 1.71 (m, 4H), 1.39 (m, 4H), 1.26 (m, 4H), 1.06~1.18 (m, 12H).

ESI-MS: m/z = 671.16 (Calculated for $C_{34}H_{43}N_2O_2Br_2^+$: m/z = 671.17)

Compound 1 (0.25 g, 0.37 mmol) and trimethylamine (3.2 mmol dissolved in 1 mL methanol) were mixed in 35 mL DMF. The resulting mixture was then stirred at 90 °C overnight. And then the solution was added dropwise into 150 mL of diethyl ether. The orange solid precipitate (DPP) was filtered and washed by CH_2Cl_2 and diethyl ether. The yield was 90%.

^{1}H NMR (400 MHz, DMSO-d6, 25 °C, TMS): 7.80~7.86 (m, 4H), 7.57~7.66 (m, 6H), 3.71 (t, *J* = 7.3 Hz, 4H), 3.19~3.27 (m, 4H), 3.03 (s, 18H), 1.60 (m, 4H), 1.41 (m, 4H) 1.08~1.22 (m, 16H).

ESI-MS: m/z = 314.23 (Calculated for $C_{40}H_{60}N_4O_2^{2+}$: m/z = 314.24).

2.2 Synthesis of DPPC6

3,6-Diphenyl-2,5-dihydropyrrolo[3,4-c]pyrrole-1,4-dione (0.5 g, 1.73 mmol) and 4.16 mmol NaH (~2.4 equivalent) were added into 15 mL anhydrous DMF. The mixture was stirred until there was no bubble of H_2 generated anymore. Then 1,6-dibromohexane (3.2 mL, 19.5 mmol) was added. The reaction mixture was continued stirring overnight at 85 °C. After being cooled to room temperature, the reaction mixture was instilled into water and extracted by dichloromethane for three times. Then the dichloromethane phase was collected, washed with water for two times and dried with Na_2SO_4 for 3 h. The solution was filtered and the solvent was evaporated. The crude product was further purified using silica gel column chromatography with the solution of CH_2Cl_2: Hexane = 3:1 as eluent to result in an orange powder (Compound 2). The yield was 42%.

^{1}H NMR (400 MHz, DMSO-d6, 25 °C, TMS): 7.76~7.82 (m, 4H), 7.50~7.57 (m, 6H), 3.76 (t, *J* = 7.6 Hz, 4H), 3.33 (t, *J* = 7.2 Hz, 4H), 1.77 (m, 4H), 1.60 (m, 4H), 1.36 (m, 4H), 1.26 (m, 4H).

Compound 2 (0.20 g, 0.31 mmol) and trimethylamine (3.2 mmol dissolved in 1 mL methanol) were mixed in 30 mL DMF. The resulting mixture was then stirred at 90 °C overnight. And then the solution was added dropwise into 150 mL of diethyl ether. The orange solid precipitate (DPPC6) was filtered and washed by CH_2Cl_2 and diethyl ether. The yield was 83%.

^{1}H NMR (400 MHz, DMSO-d6, 25 °C, TMS): 7.82~7.86 (m, 4H), 7.60~7.63 (m, 6H), 3.72 (t, *J* = 7.6 Hz, 4H), 3.14~3.18 (m, 4H), 2.97 (s, 18H), 1.55 (m, 4H), 1.43 (m, 4H) 1.09~1.21 (m, 16H).

ESI-MS: m/z = 286.20 (Calculated for $C_{40}H_{60}N_4O_2^{2+}$: m/z = 286.20).

2.3 Synthesis of DPPC10

3,6-Diphenyl-2,5-dihydropyrrolo[3,4-c]pyrrole-1,4-dione (0.5 g, 1.73 mmol) and 7.00 mmol NaH (~4.0 equivalent) were added into 15 mL anhydrous DMF. The mixture was stirred until there was no bubble of H_2 generated anymore. Then 1,10-dibromodecane (3.2 mL, 14.0 mmol) was added. The reaction mixture was continued stirring overnight at 60 °C. After being cooled to room temperature, the reaction mixture was instilled into water and extracted by dichloromethane for three times. Then the dichloromethane phase was collected, washed with water for two times and dried with Na_2SO_4 for 3 h. The solution was filtered and the solvent was evaporated. The crude product was further purified using silica gel column chromatography with the solution of CH_2Cl_2 as eluent to result in an orange powder. The orange powder (Compound 3) was washed by pure hexane and dried. The yield was 11%.

^{1}H NMR (400 MHz, DMSO-d6, 25 °C, TMS): 7.79~7.82 (m, 4H), 7.52~7.56 (m, 6H), 3.74 (t, *J* = 7.5 Hz, 4H), 3.39 (t, *J* = 7.2 Hz, 4H), 1.83 (m, 4H), 1.53~1.61 (m, 8H), 1.38 (m, 4H), 1.16~1.27 (m, 16H).

Compound 3 (0.21 g, 0.29 mmol) and trimethylamine (2.0 mmol dissolved in 1 mL THF) were mixed in 30 mL DMF. The resulting mixture was then stirred at 90 °C overnight. And then the solution

was added dropwise into 150 mL of diethyl ether. The orange solid precipitate (DPPC10) was filtered and washed by diethyl ether. The yield was 90%.

^{1}H NMR (400 MHz, DMSO-d6, 25 °C, TMS): 7.80~7.84 (m, 4H), 7.58~7.63 (m, 6H), 3.69 (t, *J* = 7.5 Hz, 4H), 3.18~3.27 (m, 4H), 3.02 (s, 18H), 1.63 (m, 4H), 1.40 (m, 4H) 1.05~1.28 (m, 24H).

ESI-MS: m/z = 342.27 (Calculated for $C_{40}H_{60}N_4O_2^{2+}$: m/z = 342.27).

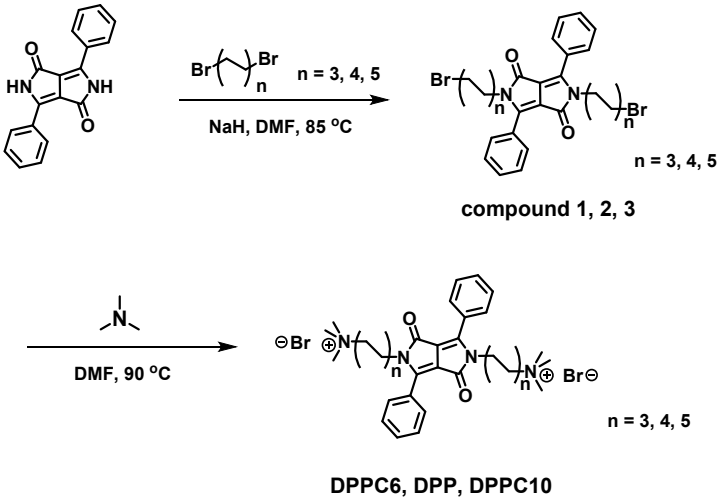

Figure S1. Synthetic routes of DPPC6, DPP and DPPC10.

3. Spectroscopic properties of DPP, DPP/(CB[7])$_2$ and DPP/(CB[8])$_2$ in aqueous solution

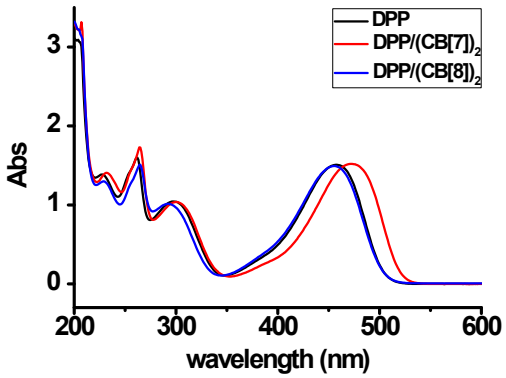

Figure S2. The UV-Vis spectra of DPP, DPP/(CB[7])$_2$ and DPP/(CB[8])$_2$ (0.1 mM in distilled water).

The absorption peak of DPP/(CB[7])$_2$ has a 10 nm red shift compared with DPP itself, while the absorption peak of DPP/(CB[8])$_2$ is similar to DPP itself. This difference is most likely to be attributed to the different supramolecular structures. As shown in Figure 6 and Figure S15, the torsional angles between the DPP chromophore and the phenyl group are calculated to be 46.0° for DPP, 27.5° for DPP/(CB[7])$_2$ and 51.8° for DPP/(CB[8])$_2$. The smaller torsional angle in DPP/(CB[7])$_2$ leads to a larger π-conjugation , which is responsible for the red shift[1,2].

4. The color evolution of the aqueous solutions during Fenton oxidation

See Supplementary Video.

5. Detailed analysis on the Fenton oxidation kinetics of DPP, DPP/(CB[7])$_2$ and DPP/(CB[8])$_2$.

According to the basic principle of chemical kinetics, when the initial concentrations of reactants keep constant, the relationship between reaction rate (k) and half-life ($t_{1/2}$) follows:

$$t_{1/2} = \frac{C}{k} \text{ (C = constant)}$$

where $t_{1/2}$ can be obtained directly from the time-conversion curves. From our experiments, $t_{1/2}$ data at different temperatures were summarized in Table S1.

Table S1 Half-life ($t_{1/2}$) of Fenton oxidation of DPP, DPP/(CB[7])$_2$ and DPP/(CB[8])$_2$ measured by UV/Vis spectroscopy in aqueous solutions with the same concentration (0.1 mM) at different temperatures.

	DPP	**DPP/(CB[7])$_2$**	**DPP/(CB[8])$_2$**
$t_{1/2}$ at 10 °C (min)	-	-	12.4
$t_{1/2}$ at 15 °C (min)	-	-	8.1
$t_{1/2}$ at 20 °C (min)	-	162.2	5.0
$t_{1/2}$ at 25 °C (min)	1085.6	105.7	3.4
$t_{1/2}$ at 30 °C (min)	548.4	63.7	2.4
$t_{1/2}$ at 35 °C (min)	267.8	38.9	-
$t_{1/2}$ at 40 °C (min)	143.0	25.6	-
$t_{1/2}$ at 45 °C (min)	72.0	-	-

According to the Arrhenius formula:

$$k = Aexp(-\frac{E_a}{RT})$$

where E_a is the apparent activation energy, A is the pre-exponential factor, R is universal gas constant and T is temperature. Thus we can obtain:

$$\frac{C}{t_{1/2}} = Aexp(-\frac{E_a}{RT})$$

And then the equation can be further transformed to be:

$$\ln\left(t_{1/2}\right) = \frac{E_a}{R} \times \frac{1}{T} + lnC + lnA$$

From the data of half-life ($t_{1/2}$) at different temperatures (T), we can obtain the apparent activation energy (E_a) of Fenton oxidation with the linear fitting method, as shown in Figure S3.

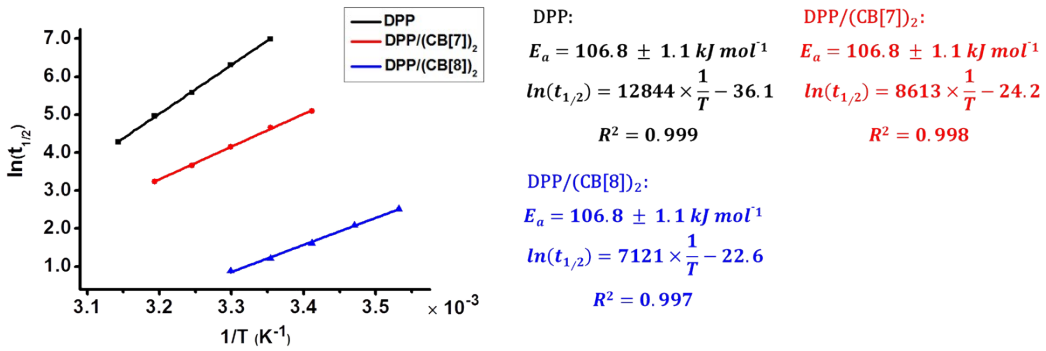

Figure S3. Linear fitting of the half-life ($t_{1/2}$) to the reaction temperature (T) gives the apparent activation energy (E_a) of Fenton oxidation of DPP, DPP/(CB[7])$_2$ and DPP/(CB[8])$_2$.

6. The activation effect of cucurbituril on DPP radical cation.

To confirm the activation effect of CB[8] on DPP$^{\bullet+}$, we used UV-Vis spectroscopy to monitor the concentration of DPP$^{\bullet+}$ during the Fenton oxidation. As shown in Figure S4 (also in Figure 2a), a broad absorption band ranging from 550 to 700 nm, which is corresponding to the absorption of DPP$^{\bullet+}$, appeared during the oxidation.[3,4] Along with Fenton oxidation, the absorption peak of DPP$^{\bullet+}$ increased and then decreased until baseline. The evolution of the absorption peak of DPP$^{\bullet+}$, DPP$^{\bullet+}$/(CB[7])$_2$ and DPP$^{\bullet+}$/(CB[8])$_2$ during the oxidation process was shown in Figure S5. After the introduction of CB[7] or CB[8], the concentration of DPP$^{\bullet+}$ was clearly decreased, indicating that DPP$^{\bullet+}$ was less accumulated.

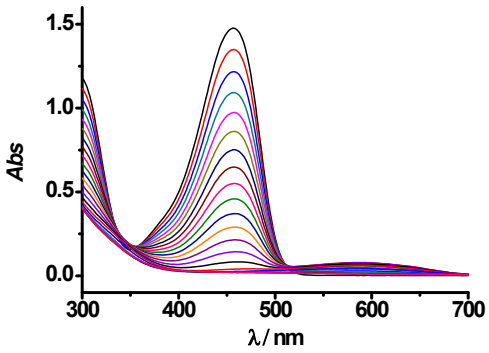

Figure S4. The oxidation kinetics of 0.1 mM DPP in 0.1 mM Fe^{3+} and 10mM H_2O_2 at 25 °C. The broad absorption peak from 550 nm to 700 nm was clearly observed.

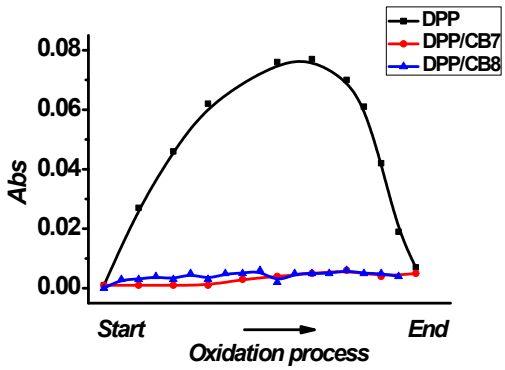

Figure S5. Evolution of the concentration of DPP$^{\bullet+}$, DPP$^{\bullet+}$/(CB[7])$_2$ and DPP$^{\bullet+}$/(CB[8])$_2$ throughout the oxidation process.

A similar phenomenon was observed using EPR spectroscopy (Figure S6). The EPR signal of $DPP^{\bullet+}$ with $g = 2.0031$ was observed after half of the Fenton oxidation.[5] In the system of DPP/$(CB[7])_2$ and DPP/$(CB[8])_2$, no explicit EPR signal could be observed because of the low concentration during the oxidation process. There could be due to two possible reasons. First, the introduction of CB[7] or CB[8] inhibits the generation of $DPP^{\bullet+}$. The other one is that the introduction of CB[7] or CB[8] accelerates the consumption of $DPP^{\bullet+}$. Considering the acceleration of Fenton oxidation, the second one is more reasonable than the first one.

The concentration of $DPP^{\bullet+}$ after the introduction of CB[7] was already too low to be detected. From either the UV-Vis spectra or the ESR spectra, no significant change of the concentration of $DPP^{\bullet+}$ during the oxidation was observed after the introduction of CB[7] and CB[8]. However, from the greater acceleration behavior of CB[8], we can deduce that the $DPP^{\bullet+}$ is further activated by CB[8] than CB[7]. Further detailed discussion using theoretical modeling is presented below.

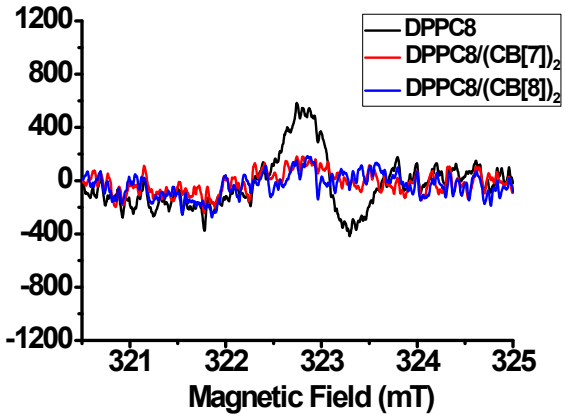

Figure S6. EPR spectra of $DPP^{\bullet+}$, $DPP^{\bullet+}$/$(CB[7])_2$ and $DPP^{\bullet+}$/$(CB[8])_2$ after half of the total reaction time of the oxidation process.

7. Detailed analysis of the oxidation products of DPP, DPP/$(CB[7])_2$ and DPP/$(CB[8])_2$

The comparison of the oxidation products of DPP, DPP/$(CB[7])_2$ and DPP/$(CB[8])_2$ after 24 hours were shown in Figure S7. From the ^{1}H-NMR spectra, we can find that considerable amount of aliphatic products and some aromatic products still remained. For DPP/$(CB[7])_2$, little aromatic products could be observed and the concentrations of aliphatic products were lower than the degradation products of naked DPP. The sharp peak at 3.17 ppm refers to the signal of CH_3OD in CB[7]. For DPP/$(CB[8])_2$, no clear signal of any aromatic products were observed and the amount of aliphatic products were limited as well.

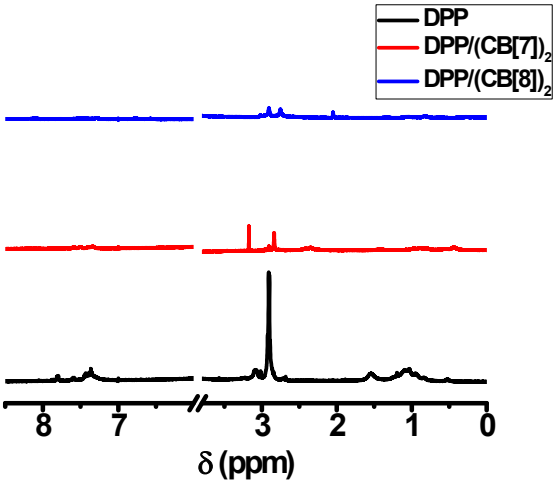

Figure S7. The ^{1}H-NMR spectra of the oxidation products of DPP, DPP/(CB[7])$_2$ and DPP/(CB[8])$_2$ after 24 h. (1 mM in D_2O).

The oxidation products of DPP were also analyzed by ESI-MS spectrum. In Figure S8, some possible products were listed.

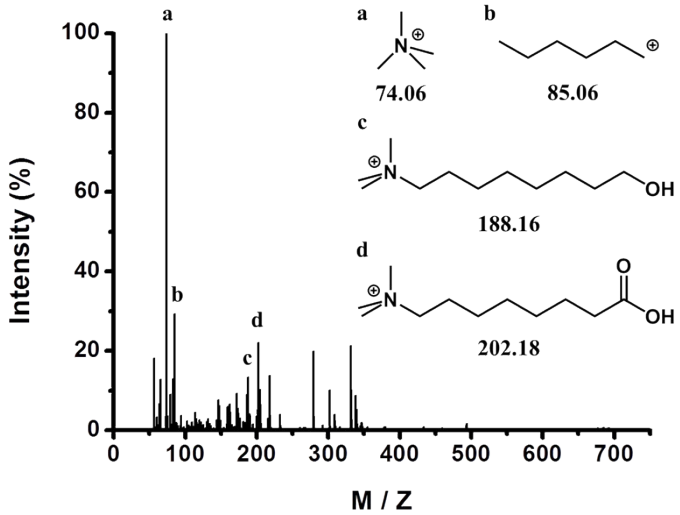

Figure S8. ESI-MS spectrum of the oxidation products of DPP and some estimated products.

8. Supramolecular structure of DPP/(CB[7])$_2$ in aqueous solution

The structure of DPP/(CB[7])$_2$ was shown in Figure S9. According to the ^{1}H-NMR, after the introduction of CB[7], the signals of proton a, b shifted downfield and proton c ~ h shifted upfield, indicating that the alkyl chain was encapsulated into the cavity of CB[7]. ITC indicated that DPP formed a 1:2 supramolecular complex with CB[7] and the binding constant was 6.4×10^5 M^{-1} (Figure S10).

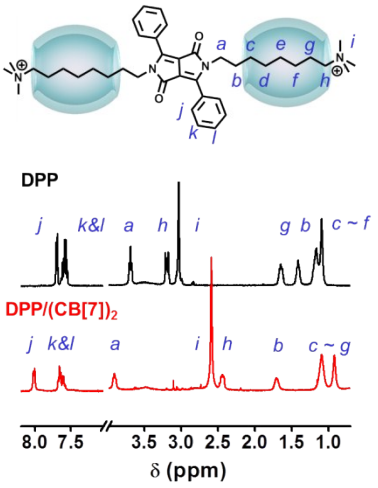

Figure S9. The structure and ^{1}H-NMR spectra of DPP/(CB[7])$_2$ (1mM in D_2O).

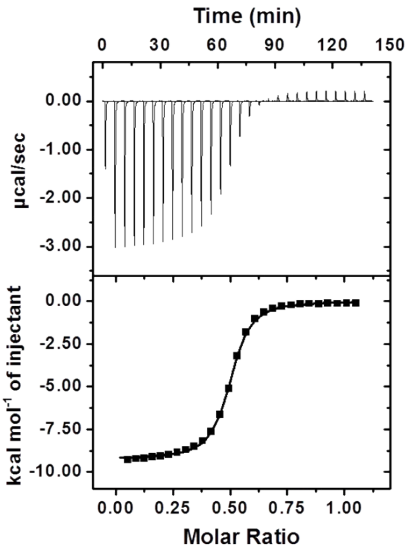

Figure S10. ITC data and fitting curve for the titration of DPP (1.0 mM) into CB[7] (0.20 mM).

9. The ROESY of DPP/(CB[8])$_2$ and naked DPP without CB[8].

According to Figure S11, the four cross-peaks between protons b, c and protons k, l in DPP/(CB[8])$_2$ could also be observed at the opposite region of ROESY spectrum (Figure 5c). The cross-peaks of proton b, c and proton l were covered by the strong noise of proton l.

The partial ROESY of naked DPP without CB[8] was measured as a control (Figure S12), the four cross-peaks between protons b, c and protons k, l were not observed.

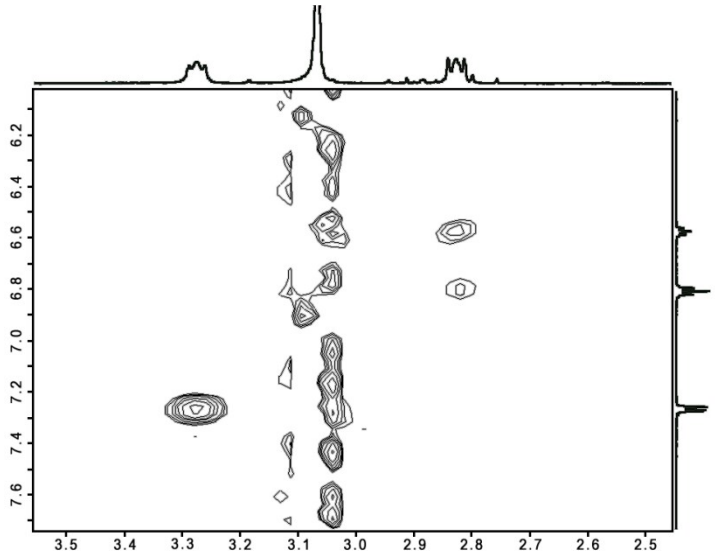

Figure S11. Partial ROESY of DPP/$(CB[8])_2$ (1 mM in phosphate buffer, pH = 7.0)

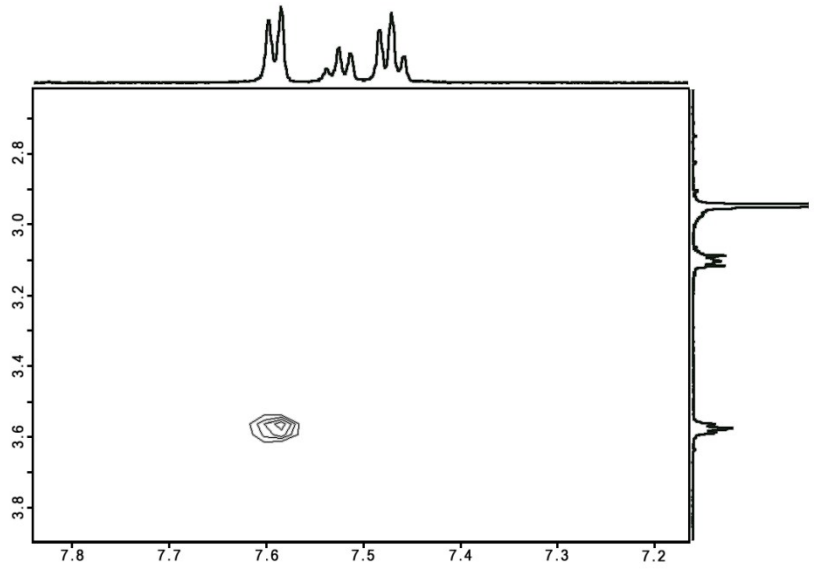

Figure S12. Partial ROESY of DPP without the addition of CB[8] (1 mM in phosphate buffer, pH = 7.0)

10. The supramolecular activation capacity and the distance between the spin center of radical cation and carbonyl groups of cucurbit[n]uril.

To investigate the generality of this supramolecular activation strategy based on the formation of folded conformation complex, we synthesized a series of DPP derivatives with different chain lengths, containing DPPC6, DPP and DPPC10. For DPPC6/$(CB[7])_2$, the acceleration ratio was 1.7 times and for DPPC10/$(CB[7])_2$, it was 4.9 times. From this point of view, the acceleration ratios of Fenton oxidation were not high enough and easily affected by the length of alkyl chain. However, compared with CB[7], the introduction of CB[8] showed much higher acceleration ratios of Fenton oxidation, which was 28 times for DPPC6/$(CB[8])_2$ and 32 times for DPPC10/$(CB[8])_2$. The structures of DPPC6/$(CB[8])_2$ and DPPC10/$(CB[8])_2$ were similar to DPP/$(CB[8])_2$, both the phenyl groups and alkyl chains were encapsulated, as confirmed by ^{1}H NMR, ITC and theoretical modeling (Figure S13, S14 and S15). The binding constant of DPPC10/$(CB[8])_2$ was 2.5×10^5 M^{-1} and the binding constant of

DPPC6/$(CB[8])_2$ was 2.5×10^6 M^{-1} (Figure S14). Therefore, for DPP derivatives with different chain lengths, the introduction of CB[8] exhibited a clear effect of activation on DPP radical cation, inducing an efficient acceleration of Fenton oxidation.

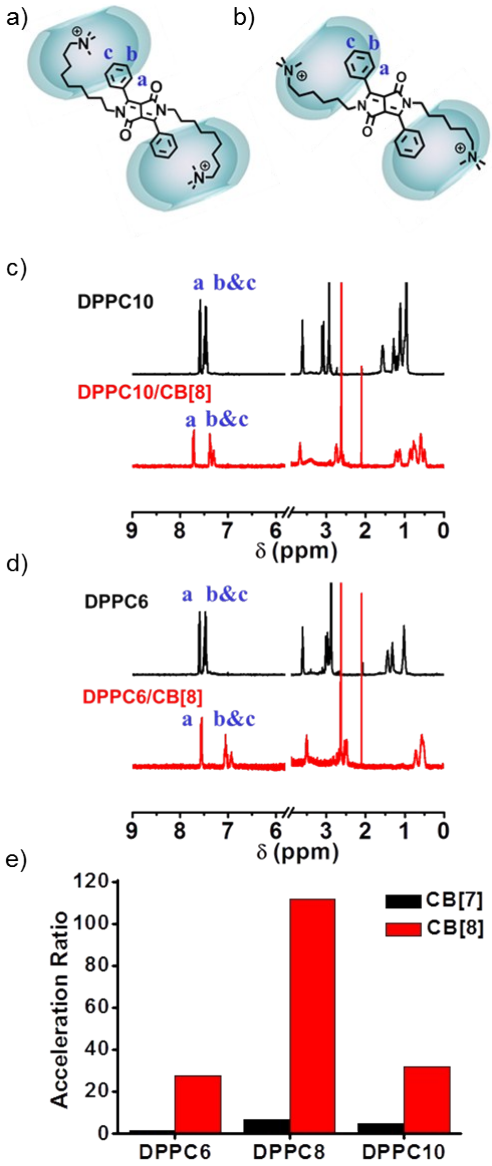

Figure S13. The structure of a) DPPC10/$(CB[8])_2$ and b) DPPC6/$(CB[8])_2$. The ^{1}H-NMR spectra of c) DPPC10/$(CB[8])_2$ and d) DPPC6/$(CB[8])_2$. (e) The comparison of acceleration ratios of different DPP derivatives' complex with CB[7] and CB[8].

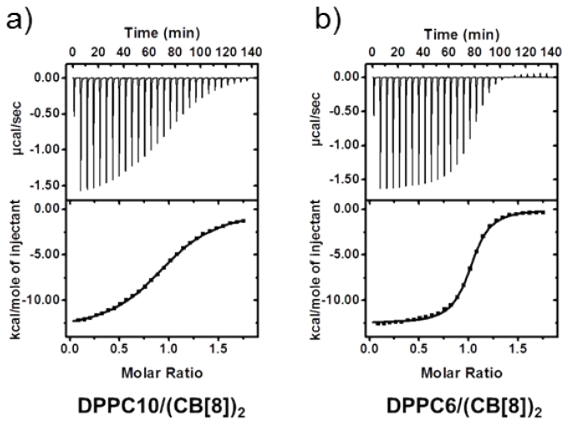

Figure S14. ITC curve of DPPC10/$(CB[8])_2$ and DPPC6/$(CB[8])_2$ (in NaAc/HAc buffer, pH = 4.75).

11. Computational details and theoretical results

The aforementioned supramolecular systems are rather bulky. We adopted a QM/MM approach that combines the accuracy of quantum mechanics (QM) and efficiency of classic molecular mechanism (MM).[6,7] We used TIP3P model[8] for water and GAFF99SB force field[9] for DPP(C6, C8, C10), CB[7] and CB[8] moieties implemented from AmberTools16 package.[10] Since the whole system has three positive ions, we induced three Cl^- counter-ions for the purpose of charge-balance. The QM/MM calculations were done with the ChemShell package[11] using Gaussian 03[12] for the QM part and DL-POLY[13] for the MM part. All of the reported geometries were fully optimized with the DL-FIND optimizer.[14] Unrestricted Kohn-Sham density functional theory with the BP86 GGA functional.[15,16] and 6-31G(d) basis sets were applied in the QM calculations. The optimized structures of DPP, DPP/$(CB[7])_2$, DPP/$(CB[8])_2$, DPPC6/$(CB[8])_2$ and DPPC10/$(CB[8])_2$ are displayed in Figure S15 for comparison, where the water environment and counter-ions are not shown for visual clarity.

The single-point full-QM calculation using the optimized geometries generated from QM/MM method was performed at the level of density functional theory (DFT) using ADF 2016.101 quantum chemistry software[17] to get atomic charges, spin densities, and MO one-electron energy levels. The spin densities of each system are shown in Figure S16 in detail. We used GGA PBE[18] exchange-correlation functional and the scalar-relativistic zero-order regular approach (ZORA).[19] Charge embedded model was adopted to treat the CB[8] rings and the frozen core approximation with polarized triple-zeta (TZP) basis sets were applied for the DPP chains.[20]

11.1 Determination of the stable structure

From our geometry optimizations at the level of QM/MM approach, the stable structures of each radical are determined and are displayed in Figure S15. CB[8] ring is larger so that it can capsulate the phenyl moieties, giving rise to smaller distance between the nearest oxygen atoms on CB rings and the unpaired electron center. In terms of the longer DPP chains, such as DPP and DPPC10, the DPP chain is bent in the terminal region due to the attraction force of opposite charges.

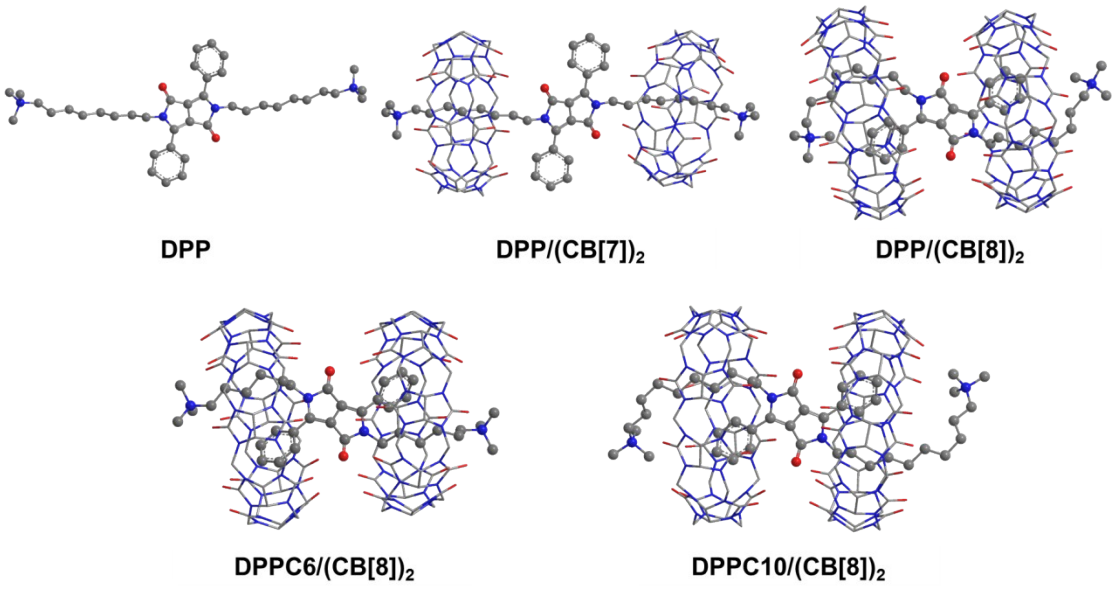

Figure S15. Optimized structures of DPP, DPP/$(CB[7])_2$, DPP/$(CB[8])_2$, DPPC6/$(CB[8])_2$ and DPPC10/$(CB[8])_2$ obtained from QM/MM method (H atoms on the DPP chains are visually omitted for simplicity, the water environment and counter-ions are not shown here).

11.2 Detailed study on the electrostatic effect of cucurbit[n]uril

The reactive activity of free radicals can be modulated via electrostatic potentials from the environment. As is shown, the ability of electron-withdrawing from CB[n] ring induced by electrostatic contribution affects the reactivity of the DPP radical. Thus we calculated the Mulliken spin distributions for each supramolecular cation for a systematical comparison, as plotted in Figure S16. Detailed distributions on each C atom in the central conjugated ring of DPP are listed in Table S2. A distinct and remarkable trend was found that the localization degree of the single radical is the most in DPP/$(CB[8])_2$ system, consistent with highest oxidation rate via the experimental observation.

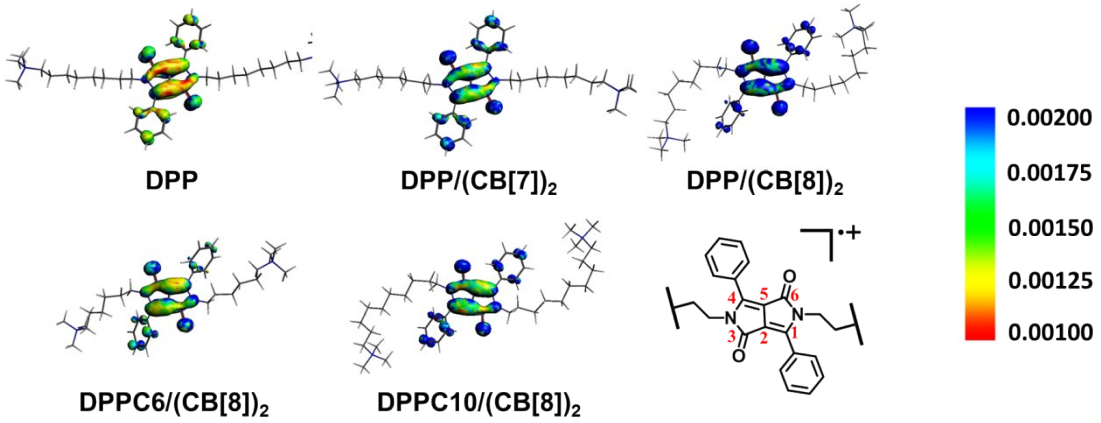

Figure S16. Spin densities of each system with the range from 0.001 to 0.002.

Table S2 Calculated spin distribution of the six C atoms in the central aromatic ring (C1-C6 as numbered in Figure 7a and Figure S16)

	DPP	**DPP/(CB[7])$_2$**	**DPP/(CB[8])$_2$**	**DPPC6/(CB[8])$_2$**	**DPPC10/(CB[8])$_2$**
C1	0.1328	0.1867	0.2370	0.1457	0.1851
C2	0.0497	0.0825	0.1157	0.0707	0.0912
C3	0.0052	0.0014	0.0013	0.0031	0.0081
C4	0.1248	0.1752	0.2252	0.1482	0.1568
C5	0.0375	0.0986	0.0998	0.0940	0.1120
C6	0.0068	0.0026	0.0076	0.0055	0.0156
Sum	0.3568	0.5470	0.6866	0.4960	0.5688

From molecular dynamic theory, total energy function can be predominately expressed as:

$$E = E_{\text{bond}} + 4\varepsilon_{ij}\left[\left(\frac{\sigma_{ij}}{r_{ij}}\right)^{12} - \left(\frac{\sigma_{ij}}{r_{ij}}\right)^{6}\right] + \sum_{i}\sum_{j\neq i}\frac{q_i q_j}{\varepsilon r_{ij}} + \ldots$$

Here E_{bond} is bonded interaction terms, composed of bond stretching, bond-angle bending, torsional dihedral and out-of-plane distortion contributions. The second term corresponds to the fast-attenuating van der Waals interaction, and the last term is the energy due to electrostatic potential. The distances between the bilateral N atom of the DPP conjugated region and the nearest O atoms derived from carbonyls of CB[n] rings are measured to be about 3.6 Å, which is far beyond the sum (~3.07 Å) of the van der Waals radii of N and O atoms and precludes any significant bonding or van der Waals interactions. This result gives rise to indirect evidence of the non-bonded electrostatic effect of CB[n] modulating the spin distribution and accelerating the oxidation reaction rate. As has been shown, the calculated SOMO energies and localization of the free radical electron are indeed significantly affected by the electrostatic potentials from the bulky supramolecular ligands.

Reference

1 C. Kanimozhi, M. Naik, N. Yaacobi-Gross, E. K. Burnett, A. L. Briseno, T. D. Anthopoulos and S. Patil, *J. Phys. Chem. C*, 2014, **118**, 11536.

2 C. B. Nielsen, M. Turbiez and I. McCulloch, *Adv. Mater.*, 2013, **25**, 1859.

3 S. Luňák, Z. Eliáš, T. Mikysek, J. Vyňuchal and J. Ludvík, *Electrochim. Acta*, 2013, **106**, 351.

4 P. E. Hartnett, S. M. Dyar, E. A. Margulies, L. E. Shoer, A. W. Cook, S. W. Eaton, T. J. Marks and M. R. Wasielewski, *Chem. Sci.*, 2015, **6**, 402.

5 M. Gora, S. Pluczyk, P. Zassowski, W. Krzywiec, M. Zagorska, J. Mieczkowski, M. Lapkowski and A. Pron, *Synth. Met.*, 2016, **216**, 75.

6 A. Warshel and M. Levitt, *J. Mol. Biol.*, 1976, **103**, 227.

7 E. Brunk and U. Rothlisberger, *Chem. Rev.*, 2015, **115**, 6217.

8 W. L. Jorgensen, J. Chandrasekhar, J. D. Madura, R. W. Impey and M. L. Klein, *J. Chem. Phys.*, 1983, **79**, 926.

9 J. Wang, R. M. Wolf, J. W. Caldwell, P. A. Kollman and D. A. Case, *J. Comput. Chem.*, 2004, **25**, 1157.

10 R. M. B. D. A. Case, D. S. Cerutti, T. E. Cheatham III, T. A. Darden, R. E. Duke, T. J. Giese, H. Gohlke, A. W. Goetz, N. Homeyer, S. Izadi, P. Janowski, J. Kaus, A. Kovalenko, T. S. Lee, S. LeGrand, P. Li, C. Lin, T. Luchko, R. Luo, B. Madej, D. Mermelstein, K. M. Merz, G. Monard, H.

Nguyen, H. T. Nguyen, I. Omelyan, A. Onufriev, D. R. Roe, A. Roitberg, C. Sagui, C. L. Simmerling, W. M. Botello-Smith, J. Swails, R. C. Walker, J. Wang, R. M. Wolf, X. Wu, L. Xiao and P.A. Kollman, *(2016), AMBER 2016, University of California, San Francisco*.

11 ChemShell, a Computational Chemistry Shell, see www.chemshell.org.

12 H. B. Schlegel, G. E. Scuseria, M. A. Robb et al., Gaussian03, revision C. 02[J]. Gaussian, Inc.: Wallingford, CT, 2004.

13 W. Smith and T. R. Forester, *J. Mol. Graph.*, 1996, **14**, 136.

14 J. Kästner, J. M. Carr, T. W. Keal, W. Thiel, A. Wander and P. Sherwood, *J. Phys. Chem. A*, 2009, **113**, 11856.

15 J. P. Perdew, *Phys. Rev. B*, 1986, **33**, 8822.

16 A. D. Becke, *Phys. Rev. A*, 1988, **38**, 3098.

17 ADF and SCM, Theoretical Chemistry, Vrijie Universiteit, Amsterdam, The Netherlands, 2016, http://www.scm.com., (http://www.scm.com).

18 J. P. Perdew, K. Burke and M. Ernzerhof, *Phys. Rev. Lett.*, 1996, **77**, 3865.

19 E. Van. Lenthe, E. J. Baerends and J. G. Snijders, *J. Chem. Phys.*, 1993, **99**, 4597.

20 E. Van. Lenthe and E. J. Baerends, *J. Comput. Chem.*, 2003, **24**, 1142.